Solar Phys (2019) 294:99
https://doi.org/10.1007/s11207-019-1492-9

EDITOR'S CHOICE

Grand Activity Minima and Maxima *via* Dual Dynamos

Deniz Ölçek[1,2] · Paul Charbonneau[1] · Alexandre Lemerle[3] · Gabriel Longpré[1] · Florence Boileau[1]

Received: 1 October 2018 / Accepted: 3 July 2019 / Published online: 24 July 2019

Abstract Reconstructions of past solar activity based on cosmogenic radioisotopes have reaveled that the Sun spends a significant fraction ($\approx 20\%$) of its time in aperiodically recurring states of so-called Grand Minima or Grand Maxima, namely epochs of strongly supressed and markedly above-average levels of magnetic activity, respectively. The physical origin of these episodes is not yet understood. In this article we present a dual-dynamo model of the solar cycle, combining a dominant dynamo based on differential-rotation shear and surface decay of bipolar active regions, and a weak, deep-seated turbulent dynamo. The resulting dynamo simulations are found to exhibit the equivalent of observed Grand Minima and Maxima. By adjusting the magnitude and saturation level of the secondary turbulent dynamo, we can reproduce well the duration and waiting-time distributions of Grand Minima and Maxima inferred from the cosmogenic-isotope record. The exit from Grand Minima episodes is typically characterized by strong hemispheric asymmetries, in agreement with sunspot observations during the 1645 – 1715 Maunder Minimum. In these simulations, Grand Maxima can be unambiguously identified as a distinct dual-dynamo state resulting from constructive interference between the two dynamos mechanisms operating within the simulation. This interaction leads to the autonomous production of long quasi-periodicities in the millennial range, commensurate with the Halstatt cycle. Such a quasi-periodic modulation, readily produced through dynamical backreaction on large-scale flows in non-kinematic dynamo models, is quite uncommon in a purely kinematic solar-cycle model such as the one developed herein. We argue that these long periodicities are set by the long diffusion time of magnetic field accumulating in the stable layers underlying the turbulent convection zone.

✉ D. Ölçek
deniz.olcek@mcgill.ca

1 Département de physique, Université de Montréal, 2900 boul. Edouard-Montpetit, Montréal, QC, H3T 1J4, Canada

2 Present address: Department of Physics, McGill University, 3600 University Street, Montréal, QC, H3A 2T8, Canada

3 Collège de Bois-de-Boulogne, 10555 av. Bois-de-Boulogne, Montréal, QC, H4N 1L4, Canada

Keywords Long-term solar variability · Solar dynamo · Babcock–Leighton mechanism · α-Effect · Solar activity reconstruction · Grand Minimum · Grand Maximum

1. Introduction

Governing space climate in the heliosphere and structuring the Earth's upper atmospheric layer and magnetosphere, the Sun is a magnetically active star showing cyclic magnetic activity with a primary quasi-periodicity of approximately 11 years. The 400-years sunspot record reveals that the activity cycle is far from being strictly periodic, and that it exhibits long-term fluctuations (Hathaway, 2009) on decadal to at least centennial timescales. This long-term variability includes multi-decadal episodes of very low activity, during which sunspots vanish almost completely, such as the 1645 – 1715 Maunder Minimum (Eddy, 1976; Ribes and Nesme-Ribes, 1993), as well as sustained periods of markedly above-average activity, such as the 1940 – 2000 Modern Maximum (Usoskin, 2013).

The cosmogenic isotopes such as ^{10}Be in ice cores and ^{14}C in tree rings allow us to investigate long-term solar variability much farther into the past (Beer *et al.*, 1990; Usoskin, Solanki, and Kovaltsov, 2007; Knudsen *et al.*, 2009; Steinhilber *et al.*, 2012; Usoskin *et al.*, 2016b). These radioactive isotopes are being produced through spallation reactions triggered by the entry of energetic cosmic rays into the Earth's atmosphere. The cosmic-ray flux at Earth's orbit, in turn, is modulated by the strength of the heliospheric magnetic field. Hence the production rates of these isotopes show a strong inverse correlation with solar activity (Usoskin, 2017). Solar activity reconstructions based on radioisotope data (*e.g.* Solanki *et al.*, 2004; Usoskin, Solanki, and Kovaltsov, 2007) shows that the Sun went through several Maunder Minimum-like and Modern Maximum-like episodes throughout the Holocene epoch (12,000 BCE – present).

Different data sets and analyses suggest the existence of two types of Grand Minima: the *short* Maunder-like Minima, and the *long* Spörer-like Minima, spanning over a century. Overall, the Sun spends between 17% and 27% of its time in a Grand Minimum state, and between 8% and 22% of its time in a Grand Maximum state (see Usoskin, Solanki, and Kovaltsov, 2007; Inceoglu *et al.*, 2015; Usoskin *et al.*, 2016b). Analyses of the waiting-time distribution (WTD) between Grand Minima/Maxima have so far remained inconclusive, with both exponential and power-law WTD providing equally acceptable fits to the various data sets; the former being indicative of a stationary memoryless random process (*e.g.* Usoskin, Solanki, and Kovaltsov, 2007), while the latter would imply a physical process with long-term "memory" (Usoskin *et al.*, 2014; Inceoglu *et al.*, 2015). These analyses unfortunately have limited statistical significance, due to the small number of Grand Minima and Maxima events present in the extant cosmogenic-isotope record (see Usoskin, Solanki, and Kovaltsov, 2007; Usoskin, 2017; Vecchio *et al.*, 2017). Such reconstructions nonetheless provide important information regarding the mode of operation of the solar dynamo.

Broadly speaking, dynamo-based explanations of Grand Minima can be subdivided into two main classes: extreme amplitude modulation and intermittency. Under the amplitude-modulation scenarios, the same cycle operates continuously, but with large modulation of the internal field strength unfolding on timescales longer than the primary cycle. Whenever the internal field strength falls below the threshold required for the generation and destabilization of magnetic-flux ropes, sunspot production ceases and a Grand Minimum ensues. Support for this interpretation can be found in residual cyclic activity observed in the ^{10}Be record during the Maunder Minimum (Ribes and Nesme-Ribes, 1993; Beer, Tobias, and Weiss, 1998). Intermittency refers to nonlinearly or stochastically driven transition between

distinct dynamo regimes, with at least one being characterized by internal magnetic-field strength too low to generate sunspots. Support for this class of explanations comes primarily from the observed lack of characteristic timescales in the duration and inter-event waiting times of Grand Minima and Maxima. Not surprisingly perhaps, over the years many different Grand Minima/Maxima scenarios have been proposed based on (relatively) simple mean-field-like dynamo models (see Section 4 of Charbonneau, 2010, and the references therein), (also Pipin and Kosovichev, 2011; Passos *et al.*, 2014; Karak *et al.*, 2014). Grand-Minima-like events have also been observed in a few global magnetohydrodynamical simulations of convection and dynamo action (*e.g.* Augustson *et al.*, 2015; Käpylä *et al.*, 2016).

Recent modeling work carried out in the context of Babcock–Leighton dynamo models suggests that the primary source of cycle fluctuations is associated with the scatter in tilt angles of bipolar magnetic regions (BMRs), which directly translates into variability of the surface dipole moment building up in the descending phase of sunspot cycles (*e.g.* Svalgaard, Cliver, and Kamide, 2005; Cameron *et al.*, 2010; Yeates and Muñoz-Jaramillo, 2013; Jiang *et al.*, 2014; Nagy *et al.*, 2017). This idea finds strong support in the good precursor potential of the surface dipole at solar minimum (see Petrovay, 2010, and the references therein), and in the observed impact of large active regions with extreme properties on the evolution of surface magnetism (Wang and Sheeley, 1991; Jiang, Cameron, and Schüssler, 2015; Yeates, Baker, and van Driel-Gesztelyi, 2015; Cameron and Schüssler, 2017).

In this article, we use the recently developed hybrid 2 × 2D Babcock–Leighton solar-cycle model of Lemerle and Charbonneau (2017) to investigate the circumstances under which fluctuations in emerging active-region properties, including but not limited to tilt-angle variability, can reproduce the duration and frequency of Grand Minima and Maxima inferred from the cosmogenic-isotope record. The lower operating threshold of Babcock–Leighton dynamos, associated with a minimal internal magnetic-field strength required to generate BMR emergences, requires the introduction of a secondary inductive mechanism to "kickstart" the dynamo once fallen into an extended Grand Minimum. Towards this end, we introduce a turbulent α-effect in the lower reaches of the convective envelope, as described in Section 2. The resulting hybrid dynamo succeeds in producing solar-like Grand Minima, as exemplified by the case study presented in Section 3, in which we also examine the statistical characterization of durations and inter-event waiting-time distributions for Grand Minima and Maxima. One interesting feature of this hybrid model is the intermittent production of epochs of elevated magnetic energy and sunspot emergences, which we can identify as Grand Maxima in the simulation, associated with a distinct mode of dual-dynamo operation. We briefly summarize in Section 5 results from a large set of similar simulations aimed at examining the dependence of Grand Minima/Maxima characteristics on parameters of the model. We conclude in Section 6 by summarizing our most salient results, followed by a critical discussion of their relevance to our understanding of long-timescale variations in the magnetic activity of the real Sun.

2. A Hybrid Solar Dynamo Model

2.1. A 2 × 2D Babcock–Leighton Dynamo

In this section, we first describe the principal elements of the solar-cycle model of Lemerle and Charbonneau (2017, hereafter LC17), on which the foregoing simulations are based (see also Lemerle, Charbonneau, and Carignan-Dugas, 2015). The model is a kinematic mean-field-like dynamo relying on differential-rotation shear to generate the large-scale toroidal

magnetic component, and on the surface decay of bipolar magnetic regions (the so-called Babcock–Leighton mechanism) to regenerate the poloidal large-scale magnetic component.

The solar interior and photospheric plasma is non-relativistic and dominated by collisions. The inductive effects of flow $\boldsymbol{u}$ on a magnetic field $\boldsymbol{B}$ are then expected to be well-described by the single-fluid magnetohydrodynamical induction equation:

$$\frac{\partial \boldsymbol{B}}{\partial t} = \nabla \times (\boldsymbol{u} \times \boldsymbol{B} - \eta \nabla \times \boldsymbol{B}), \tag{1}$$

where $\eta = 1/\mu_0 \sigma$ is the magnetic diffusivity, inversely proportional to the electrical conductivity $[\sigma]$. In modeling the solar cycle, $\boldsymbol{B}$ is identified with the large-scale, axisymmetric component of the solar magnetic field, the large-scale flow $[\boldsymbol{u}]$ is considered given and includes contributions from differential rotation and meridional circulation, and η includes a macroscopic contribution from unresolved scales of fluid motions, namely small-scale turbulent flows associated with thermally driven convection.

Formulated in spherical polar coordinates $[r, \theta, \phi]$, the originality of the LC17 model lies in solving concurrently two coupled geometrically simplified forms of Equation 1, each in two spatial dimensions. The first is a 2D kinematic flux transport dynamo (FTD) model (see, *e.g.*, Dikpati and Charbonneau, 1999; Karak *et al.*, 2014) for the temporal evolution of an axisymmetric $[\partial/\partial\phi \equiv 0]$, magnetic field described by a toroidal component $[\boldsymbol{B} = B(r, \theta, t)\hat{\mathbf{e}}_\phi]$, and a toroidal vector potential $[\boldsymbol{A} = A(r, \theta, t)\hat{\mathbf{e}}_\phi]$ defining the poloidal component *via* $\nabla \times (A\hat{\mathbf{e}}_\phi)$. The (steady) flow is written as

$$\boldsymbol{u}(r, \theta) = \boldsymbol{u}_\mathrm{P}(r, \theta) + \varpi\, \Omega(r, \theta)\hat{\mathbf{e}}_\phi, \tag{2}$$

with $\boldsymbol{u}_\mathrm{P}$ the flow component in meridional plane, Ω the angular velocity, and $\varpi = r \sin\theta$. Further assuming the net magnetic diffusivity $[\eta]$ to depend only on radius, Equation 1 separates into

$$\frac{\partial A}{\partial t} = -\frac{1}{\varpi}(\boldsymbol{u}_\mathrm{P} \cdot \nabla)(\varpi A) + \eta\left(\nabla^2 - \frac{1}{\varpi^2}\right)A, \tag{3}$$

$$\frac{\partial B}{\partial t} = -\varpi\,(\boldsymbol{u}_\mathrm{P} \cdot \nabla)\left(\frac{B}{\varpi}\right) + \eta\left(\nabla^2 - \frac{1}{\varpi^2}\right)B + \varpi\left(\nabla \times (A\hat{\mathbf{e}}_\phi)\right)\nabla\Omega + \frac{1}{\varpi}\frac{\partial \varpi B}{\partial r}\frac{\partial \eta}{\partial r} - B\nabla \cdot \boldsymbol{u}_\mathrm{P}. \tag{4}$$

The parametric expressions used to set the $\Omega(r, \theta)$ and $\boldsymbol{u}_\mathrm{P}$ are given in LC17 (Section 2.1). For the radial profile of magnetic diffusivity we also retain Equation 5 in LC17:

$$\eta(r) = \eta_\mathrm{c} + \frac{\eta_\mathrm{t}}{2}\left[1 + \mathrm{erf}\left(\frac{r - R_\mathrm{c}}{\delta_c/2}\right)\right], \tag{5}$$

with $R_c/\mathrm{R}_\odot = 0.7$ the base of the convection zone, within which the turbulent diffusivity assumes a high,"turbulent" value $[\eta_\mathrm{t}]$, ramping down to a lower value $[\eta_\mathrm{c}]$ in the underlying radiative core over a layer of thickness $\delta_\mathrm{c}/\mathrm{R}_\odot = 0.05$. The high value of η in the convection zone ($r > R_\mathrm{c}$) is taken to reflect the enhanced dissipation of the large-scale magnetic field caused by small-scale convective fluid motions. Equations 3 – 4 are non-dimensionalized by using the diffusion time $\tau = \mathrm{R}_\odot^2/\eta_\mathrm{t}$ and the solar radius $\mathrm{R}_\odot$ as the time and length units, respectively, and solved in meridional slice $0 \le \theta \le \pi$ spanning $0.5 \le r/\mathrm{R}_\odot \le 1$ in radius.

The second component of the LC17 dynamo model is a conventional surface-flux transport (SFT) model (see also Wang, Lean, and Sheeley, 2002; Baumann *et al.*, 2004; Lemerle, Charbonneau, and Carignan-Dugas, 2015; Whitbread *et al.*, 2017) defined over a sphere of radius equal to the Sun's, in which the non-axisymmetric large-scale surface radial magnetic component $[B_{\rm R}(\theta,\phi,t)]$ evolves in response to advective transport by (axisymmetric) surface differential rotation $[\Omega_R(\theta)]$ and a poleward meridional flow $u_\theta(\theta)$, diffusive transport by supergranular diffusion parameterized by η_R, and with emergence of bipolar active region acting as a source $[S_{\rm BMR}]$:

$$\frac{\partial B_{\rm R}}{\partial t} = -\frac{1}{R\sin\theta}\frac{\partial}{\partial\theta}\left[u_\theta(R,\theta)B_{\rm R}\sin\theta\right] - \Omega(R,\theta)\frac{\partial B_{\rm R}}{\partial\phi} + \frac{\eta_{\rm R}}{R^2}\left[\frac{1}{\sin\theta}\frac{\partial}{\partial\theta}\left(\sin\theta\frac{\partial B_{\rm R}}{\partial\theta}\right) + \frac{1}{\sin^2\theta}\frac{\partial^2 B_{\rm R}}{\partial\phi^2}\right] - \frac{B_{\rm R}}{\tau_R} + S_{\rm BMR}(\theta,\phi,t). \quad (6)$$

In this expression $S_{\rm BMR}$ is a surface-flux source term associated with the emergence of individual bipolar magnetic regions, and $\tau_{\rm R}$ is a surface decay timescale modeling convective submergence.

The full dynamo model is constructed by coupling these FTD and SFT modules; at a given time step, integrating the azimuthal average of the SFT-generated $B_{\rm R}(\theta,\phi,t)$ yields a surface latitudinal distribution of the vector potential $A(R,\theta,t)$ providing a time-evolving upper boundary condition on A in the FTD module. This boundary driving effectively acts as a source term on the RHS of Equation 3. The internal distribution of magnetic fields in the FTD module at a given time step, in turn, is used to construct an "emergence function" giving the probability of triggering a BMR emergence in the SFT module at that time step. A constant scaling factor $[K\ (>0)]$ sets the probability of emerging a BMR at colatitude θ as a function of the emergence function value at the same latitude (see LC17, Section 2.4). This parameter acts as the dynamo number for the model, in the sense that it must exceed a critical value for persistent magnetic cycles to materialize. Properties of emerging BMRs (magnetic flux, pole separation, tilt with respect to the E–W line, *etc.*) are randomly drawn from statistical distributions constructed from magnetographic observations spanning Cycle 21 (see the appendix of Lemerle, Charbonneau, and Carignan-Dugas, 2015, for details).

Two nonlinearities are included in the model, both inspired by calculations of the stability, rise, and emergence of magnetic-flux ropes under the thin-flux-tube approximation (see D'Silva and Howard, 1993; Caligari, Moreno-Insertis, and Schüssler, 1995; Fan, 2009). The first is a lower threshold on the emergence function, below which the emergence probability vanishes. The second is a reduction, with increasing internal magnetic-field strength, of the tilt angle between the line segment joining the two poles of the BMR and the E–W direction (as embodied in Joy's law. See, *e.g.*, McClintock and Norton, 2013). The latter is the only amplitude-limiting nonlinearity built into the model, and is parametrized by the algebraic expression

$$\gamma(\theta;B) = \gamma_0(\theta)\frac{1}{1+(B/B_{\rm q})^2}, \quad (7)$$

where γ is the tilt angle and the $B_{\rm q} = 500$ G sets the (diffuse) field strength at which reduction of the tilt sets in. See Section 4.2 in LC17 for further details. It is critical in what follows that the lower threshold on the emergence function implies that the dynamo is not self-excited; should the internal field strength fall below this threshold for whatever reason, emergence of BMRs ceases, and then so does regeneration of the poloidal component, thus breaking the dynamo loop.

As detailed in LC17, the full coupled model involves 18 adjustable parameters, which were formally optimized to yield the optimal fit to the observed spatio–temporal distribution of BMR emergences in Cycle 21. The resulting best-fit model reproduces many features of the observed solar cycle, including some that were not used to constrain the optimization, notably the observed latitudinal variation of the surface meridional flow, as well as the good correlation between the surface dipole at the end of cycle n, and the peak amplitude of (pseudo-)sunspot-number time series of cycle $n + 1$.

Running the LC17 model under its optimal parameter settings reveals a behavior that is quite interesting in the context of Grand Minima events; every once in a while the emergence algorithm will inject in the simulation a high-flux BMR with peculiar tilt angles, either disobeying Joy's law (trailing pole closer to Equator than leading pole), or even, in more extreme cases, so-called anti-Hale polarity patterns, *i.e* an ordering of polarity opposite to that normally characterizing BMR emerging in a given hemisphere and cycle. These events are rare, but they have the potential to derail the buildup of the surface dipole (Nagy *et al.*, 2017), the *sine qua non* condition for the production of the subsequent cycle. This behavior appears robust, being also observed in other implementations of Babcock–Leighton dynamos including fluctuations in tilt angles (see, *e.g.*, Karak and Miesch, 2017). Such "rogue" BMRs are also observed occasionally on the Sun, and it has been demonstrated that a strong BMR emergence with atypical properties can affect strongly the amplitude of the next cycle and lead to episodes of unusually low/high activity (see Wang and Sheeley, 1991; Cameron and Schüssler, 2012; Jiang, Cameron, and Schüssler, 2015; Yeates, Baker, and van Driel-Gesztelyi, 2015). Figure 1 shows a representative example of such an event where the dynamo completely shuts off, for a reference run using the optimal parameter values established in LC17, with dynamo number $K = 0.48$. The top panel shows a time–latitude diagram of the zonally averaged surface radial magnetic component (color scale), on which are superposed a few isocontours of BMR emergence density. The bottom panel shows the corresponding time series of the unsigned surface dipole (black) and pseudo-sunspot number (blue; hereafter abbreviated PSSN), defined here as the monthly averaged number of emergences linearly rescaled so as to yield a measure similar in magnitude to the usual international sunspot number. Here the dynamo shuts off at $t \approx 120$ years following an unfavorable sequence of emergences in the preceeding sunspot cycle (see Nagy *et al.*, 2017, for a detailed analysis of this type of event). If the dipole becomes too weak so that shearing by differential rotation does not succeed in inducing a deep-seated toroidal component exceeding the threshold strength on the emergence function, BMRs no longer emerge, and the dipole then exponentially decays instead of reversing, as is clearly the case here for $t > 260$ years. In order to successfully restart the dynamo in such situations, an additional inductive mechanism is needed to bring the system back above threshold. This idea has been implemented in a number of extant dynamo models characterized by a lower operating threshold, including but not limited to dynamo models relying on the Babcock–Leighton mechanism of poloidal-field regeneration (*e.g.* Ossendrijver, 2000; Charbonneau, Blais-Laurier, and St-Jean, 2004; Hazra, Passos, and Nandy, 2014; Passos *et al.*, 2014; Sanchez, Fournier, and Aubert, 2014).

2.2. Adding a Turbulent Convective Dynamo

The obvious candidate for a self-excited dynamo is turbulent induction associated with cyclonic convection, as embodied in the classical α-effect (Parker, 1955; Krause and Rädler, 1980), (Section 3 in Charbonneau, 2014, and the references therein). This introduces an additional electromotive force (EMF) on the RHS of the induction equation for the large-scale field (Equation 1), of the form $\nabla \times \langle \boldsymbol{u}' \times \boldsymbol{B}' \rangle$, where primes refer to small-scale flow and field

fluctuations, unresolved on the scale of $\boldsymbol{u}$ and $\boldsymbol{B}$ in Equation 1, and in the present context the angular brackets indicate an azimuthal average. For nearly isotropic, nearly homogeneous, and weakly nonlinear MHD turbulence, the turbulent EMF can be expanded as

$$\left\langle \boldsymbol{u}' \times \boldsymbol{B}' \right\rangle \equiv \boldsymbol{\xi} = \alpha \boldsymbol{B} + \beta \nabla \times \boldsymbol{B}, \tag{8}$$

where β amounts to a turbulent magnetic diffusivity, typically much larger than the microscopic (Ohmic) magnetic diffusivity, and α is the celebrated α-effect of mean-field theory. This is a minimalistic *ansatz* for the turbulent α-effect and diffusivity, omitting effects such as turbulent pumping arising if the full tensorial form of the α-tensor were retained.

If rotational shear is assumed to dominate induction of the toroidal large-scale magnetic component (the so-called $\alpha\Omega$ dynamo approximation), then β provides the η_t in Equation 5, and Equation 3 picks up a source term on its RHS, of the form $S = \alpha B$. This can evidently lead to an exponential growth of the magnetic field, so it is common practice to introduce an *ad-hoc* amplitude-limiting nonlinearity, often in the form of algebraic α-quenching:

$$\alpha(r, \theta; B) = \frac{\alpha_L(r, \theta)}{1 + (B/B_0)^2}, \tag{9}$$

where B_0 then sets the field strength at which the α-effect becomes quenched, and the function $\alpha_L(r, \theta)$ sets the spatial extent of the associated turbulent induction. In what follows we use an α-effect concentrated in the bottom half of the convection zone, as defined by the following spatial dependency:

$$\alpha_L(r, \theta) = \alpha_0 \cos\theta \sin\theta \left[1 + \mathrm{erf}\left(\frac{r - r_1}{d_1}\right)\right]\left[1 - \mathrm{erf}\left(\frac{r - r_2}{d_2}\right)\right], \tag{10}$$

with $r_1 = 0.70\ \mathrm{R}_\odot$, $r_2 = 0.85\ \mathrm{R}_\odot$, and $d_1 = d_2 = 0.050\ \mathrm{R}_\odot$, $\mathrm{erf}(x)$ is the error function, and the coefficient α_0 set the strength of the α-effect. In the dimensionless form of the governing equations, this becomes subsumed in a secondary dynamo number $[C_\alpha = \alpha_0 \mathrm{R}_\odot/\eta_t]$ measuring the strength of turbulent induction *versus* dissipation. While Equation 10 is largely *ad hoc*, it is in part inspired by determinations of the α-effect in MHD numerical simulations, which suggest the presence of a layer characterized by a negative northern hemisphere α-effect in the lower reaches of the convection zone (Section 3 in Charbonneau, 2014, and the references therein).

Figure 2 shows a 400-year segment of a representative run of the LC17 dynamo simulation, with the weak, deep-seated, turbulent α-effect now operating concurrently with the surface Babcock–Leighton mechanism. When the latter falls below threshold, here around $t \approx 100$ years, the cycle soon stops, as on Figure 1; but field induction by the weak turbulent α-effect managed to bring the internal magnetic field back above the operating threshold of the primary (dominant) Babcock–Leighton mechanism, so that "normal" cyclic behavior resumes at $t \approx 290$ years, after a "failed restart" at $t \approx 170$ years.

The bottom panel on Figure 2 displays time series of magnetic energy integrated over the solution domain. The blue curve corresponds to the sample solution of the upper panels, while the orange curve shows the behavior of a simulation with the α-effect set to zero, but otherwise identical in its parameter settings. The exponential growth of the magnetic field driven by the α-effect following shutdown of the primary Babcock–Leighton dynamo is readily visible here. Note the two different slopes in the two quiescent intervals separated by the failed restart: in the first, the dipolar mode is excited, while in the second it is the more rapidly growing quadrupolar mode which brings the magnetic field back above threshold. Note also how the simulation with the α-effect undergoes its first shutdown *before* the pure

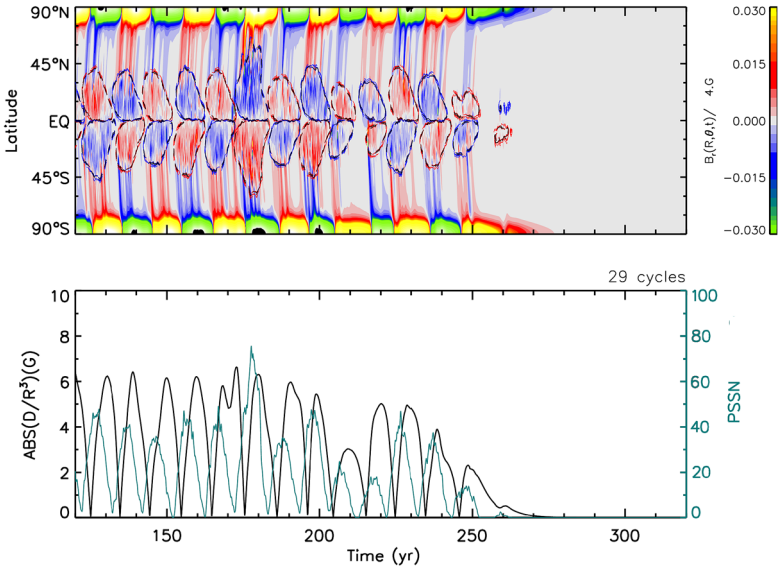

Figure 1 Time–latitude diagram of the surface radial field with superimposed isocontours of emergent BMR density (*top*), and time series of pseudo-sunspot number and absolute value of the dipole moment (*bottom*), in a representative run of the LC17 model with dynamo number $K = 0.48$. Here the dynamo shuts off at $t \approx 260$ years following an unfavorable sequence of emergences in the preceding sunspot cycle.

Babcock–Leighton simulation, evidence again that the secondary α-effect dynamo is altering the operation of the primary Babcock–Leighton dynamo, even under "normal" cyclic operation.

Acting as the sole poloidal-field regeneration mechanism, and for the differential rotation and meridional-circulation profiles adopted in the LC17 model, the resulting turbulent $\alpha\Omega$ dynamo produces a steady magnetic field peaking at mid-latitudes in the bottom half of the convection zone. In the linear regime the growth rates of the fundamental modes of antisymmetric and symmetric equatorial parity are similar, with the latter dominating in the nonlinearly saturated regime for C_α larger than about 0.28. Figure 3 shows the growth profile of the α-dynamo for various values of α_0 as well as for two different (high and low) core-diffusivity values. All simulations are initialized with the same, very weak seed magnetic field. As expected, the growth rate of an α-dynamo is greater when α_0 is larger and η_c is smaller. Hence, the values of these parameters can be expected to affect the duration of Grand Minimum episodes. Moreover, because symmetric equatorial parity is the preferred mode in most of the dynamo-number range considered in what follows, the operation of this secondary turbulent dynamo will introduce departures from the pure antisymmetric parity characterizing the original Babcock–Leighton reference dynamo solution of LC17. In order to quantify such departures we introduce a measure of equatorial parity $[P]$, defined as

$$P = \frac{B_q^2 - B_d^2}{B_q^2 + B_d^2}, \tag{11}$$

where

$$B_q = \frac{B_N + B_S}{2(B_N + B_S)}, \tag{12}$$

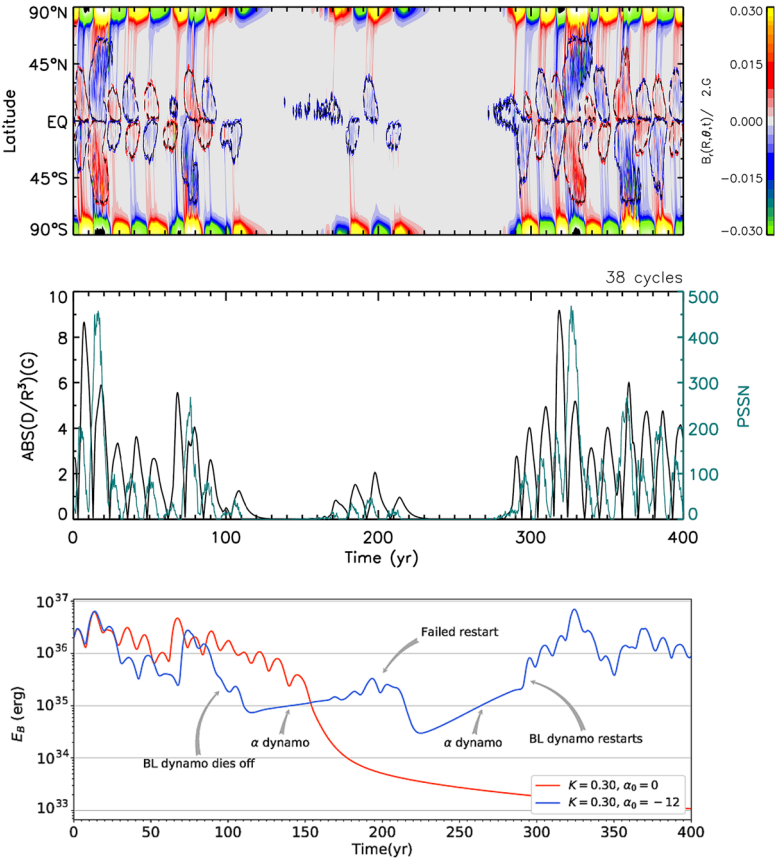

Figure 2 Segment of a representative simulation of the hybrid dynamo including the turbulent α-effect. Parameter values are $K = 0.30$, $\alpha_0 = -12$ cm s^{-1}, $B_0 = 220$ G, $B_q = 150$ G, $\eta_c = 10^8$ cm^2 s^{-1}, $\eta_t = 10^{12}$ cm^2 s^{-1}. Time–latitude diagram of the surface radial field with superimposed isocontours of emergent BMR density (*top*), time series of pseudo-sunspot number and absolute value of the dipole moment (*middle*), and corresponding time series of magnetic energy integrated over the full domain (*bottom*). The primary dynamo shuts down at $t \approx 100$ years, but restarts again at $t \approx 290$ years after a "failed restart" at $t \approx 170$ years (see text).

$$B_d = \frac{B_N - B_S}{2(B_N + B_S)}. \tag{13}$$

The quantities B_N and B_S refer to the toroidal magnetic component extracted at latitudes $\pm 30^\circ$ at the base of the connection zone ($r/R_\odot = 0.7$). Under these definitions B_q and B_p become measures of the relative magnitudes of even (quadrupole-like) and odd (dipole-like) contributions to the magnetic field. The parameter P is restricted to the range $[-1, 1]$, with $P = -1$ referring to a purely equatorially antisymmetric magnetic configuration, whereas $P = +1$ indicates a purely symmetric configuration.

2.3. Tuning the Dual Dynamo

Adjustable parameters in the reference LC17 solar-cycle model, *i.e.* without a turbulent α-effect, were formally optimized to minimize the difference between observed and sim-

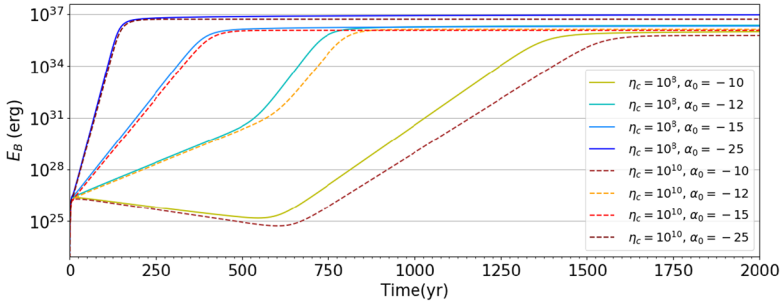

Figure 3 Different solutions of α-dynamo being the sole source term. The BL mechanism is turned off in order to investigate the relationship between the parameters α_0 and η_c, while other parameters are kept fixed ($K = 0.30$, $B_0 = 200$ G, $B_q = 150$ G, $\eta_t = 10^{12}$ cm^2 s^{-1}). The effect of core diffusivity on the growth rate of α-dynamo is explored within a range previously tested for the model by Lemerle and Charbonneau (2017). The growth α-dynamo is slightly higher when η_c is smaller.

ulated butterfly diagrams. In order to retain the good fit to observations characterizing this reference simulation, our adopted strategy is to: i) retain all optimal values of LC17 for defining parameters of the primary dynamo, allowing variations only within the error bounds resulting from the genetic-algorithm-based optimization procedure; and ii) introduce as weak a turbulent α-effect as possible, while strong enough to achieve restart of the primary dynamo. Some relatively fine tuning of the strengths and operating thresholds of the two inductive mechanisms is required to achieved the desired effect. If the turbulent α-effect is too strong, it overwhelms the Babcock–Leighton mechanisms and cyclic behavior is lost. Even for the sample solution displayed on Figure 2, it occasionally leads to a surge of mid-latitude activity, for example at $t \approx 20$ and 320 years. As argued in what follows, such episodes can plausibly be identified as Grand Maxima of solar activity.

We first examine in detail a representative dual-dynamo solution in the following section, and then turn to parameter dependencies in Section 5.

3. Case Study: Distinct Dynamo Modes in a Solar-Like Solution

With the α-effect now included as an additional inductive source, the LC17 model can now reproduce a wide variety of dynamo behaviors, some including Grand Minima and/or Grand Maxima, and others markedly non-solar. We first present and analyze in detail a simulation with parameter values yielding patterns of Grand Maxima and Minima similar to observational inferences based on cosmogenic radioisotopes. The defining parameter values are identical to those of the reference solar solution presented in LC17, with the sole exception of the (turbulent) envelope diffusivity η_t, for which a slightly reduced value is used, but still well within the confidence interval returned by the optimization procedure. We extended this simulation to 50,000 years, amounting to nearly 5000 activity cycles, in the course of which occurred of order 10^2 Grand Minima and almost as many Grand Maxima. This "case study" simulation is the focal point of this section, with the impact of parameter variations on model behavior summarized afterwards in Section 5.

Figure 4 shows a smoothed pseudo-sunspot-number time series for this 50,000 year case-study simulation. In order to facilitate comparison with reconstructions based on cosmogenic radioisotopes (Gleissberg, 1944; Mursula and Ulich, 1998; Usoskin, Solanki, and Kovaltsov, 2007), we process our simulation data in a similar manner in order to extract secular

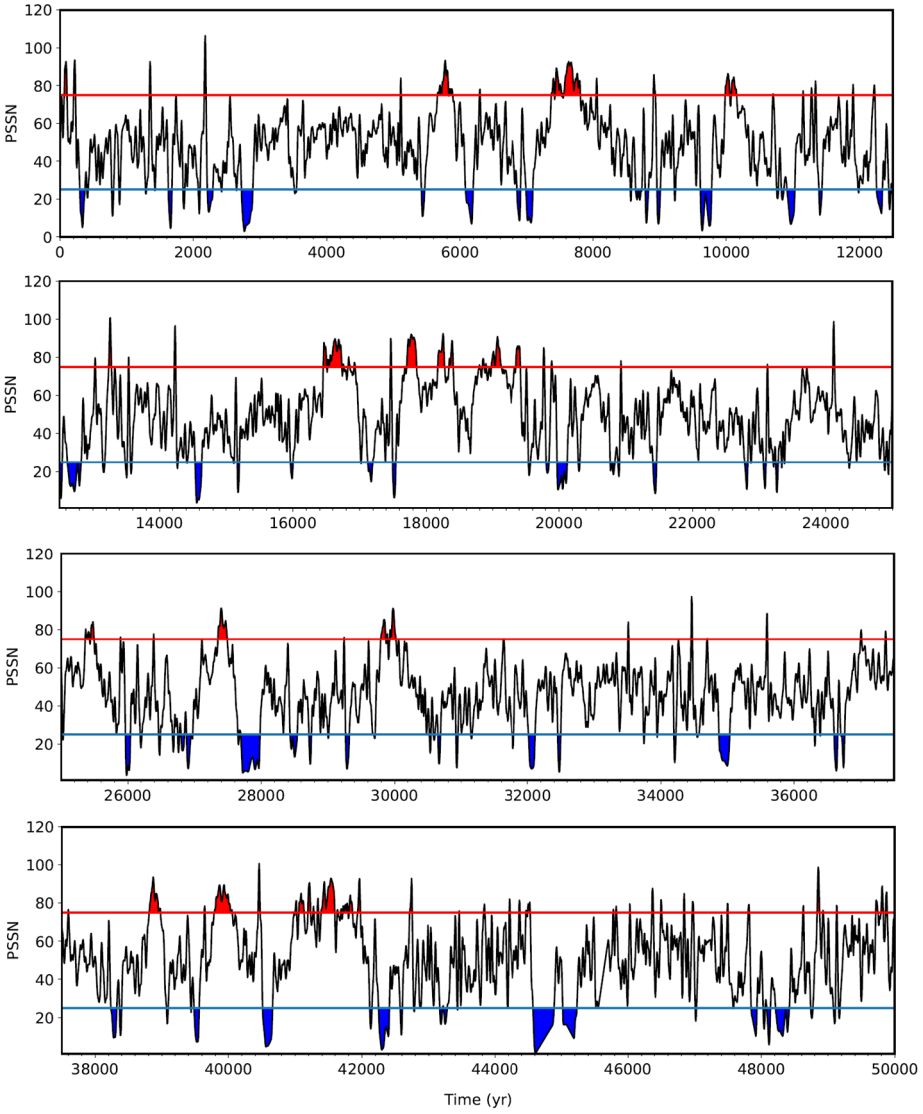

Figure 4 Smoothed pseudo-sunspot-number time series spanning 50,000 years, for a solution with $K = 0.32$, $\alpha_0 = -12$ cm s^{-1}, $B_0 = 210$ G, $B_{\rm q} = 120$ G, $\eta_c = 10^8$ cm^2 s^{-1}, $\eta_t = 10^{11.8}$ cm^2 s^{-1}. Starting from monthly PSSN values, a modulation envelope is first constructed from cycle maxima and resampled on a decadal cadence, and the resulting series smoothed with a trapezoidal 1-2-2-2-1 filter. *Blue* and *red* areas denote Grand Minima and Maxima, respectively. For ease of comparison, this plot was purposefully formatted to resemble the reconstructed activity plot inferred from the cosmogenic radioisotope record, as displayed in Figure 3 of Usoskin, Solanki, and Kovaltsov (2007).

variations. A ten-year-cadence time series is first generated by constructing a modulation envelope from cycle maxima, which is then interpolated on a fixed ten-year-step temporal grid. A trapezoidal 1-2-2-2-1 smoothing filter is then applied to this time series, the result being plotted as a solid line in Figure 4. This smoothing will lead to a slight reduction in the

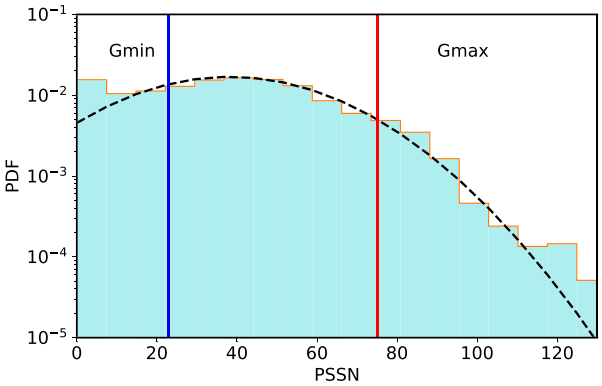

Figure 5 Histogram for sunspot-number distribution for the series in Figure 4. The *curve* represents the best-fit normal distribution while *vertical lines* correspond to the threshold values used to define Grand Minima and Grand Maxima in Figure 4.

measured durations of Grand Minima. In some cases, such as in Figure 2, two closely spaced Grand Minima separated by a brief "failed restart" will emerge as a single Grand Minimum. The smoothing also precludes the reliable identification of Grand Minima or Maxima of duration inferior to 30 years.

Again in a manner similar to the analysis the radioisotope record, we construct on Figure 5 the histogram of decadal PSSN values, and we fit it with a Gaussian (dashed line). Usoskin, Solanki, and Kovaltsov (2007) and Usoskin (2017) construct an equivalent histogram from their radioisotope-based activity reconstruction, and they choose the lower and upper points of departure from Gaussian behavior as setting the two thresholds defining their Grand Minima and Maxima. We follow this approach here, setting our lower threshold defining Grand Minima at a smoothed PSSN value of 25. Our upper threshold defining Grand Maxima is set at a value of 75, which still lies in the region of acceptable Gaussian fit on Figure 5. As discussed further below, Grand Maxima show up unambiguously in our simulations as a mode of elevated magnetic energy, mixed parity, and frequent mid-latitude BMR emergences. The time spans of these events turn out to be well delineated by a smoothed PSSN threshold of about 75. In view of our smoothing procedure, we only retain as Grand Minima/Maxima episodes during which the smoothed PSSN remains below 25 or above 75 for three consecutive cycles. These threshold values are indicated by blue and red horizontal lines in the various panels of Figure 4.

3.1. Grand Minima and Maxima

In the 50,000-year simulation depicted in Figure 4, we have identified 102 Grand Minima with a total duration of 6900 years approximately, amounting to 13.6% of the simulated time. The corresponding epochs have been colored in blue on the time series of Figure 4. Examination of the surface time–latitude diagrams reveals that in the course of many of these Grand Minima, some BMR emergences sometimes take place, either in the form of failed restarts, as in Figure 2, during which surface-dipole buildup and reversal can resume for a few decades, or more irregular emergence patterns still leaving a weak surface-dipolar signal, albeit aperiodic. This could be interpreted as residual cyclic activity, as evidenced by the ^{10}Be record throughout the Maunder Minimum (see, *e.g.*, Beer, Tobias, and Weiss, 1998).

The physical mechanism triggering onset and exit of Grand Minima are well identified in our dynamo model. Onset occurs when an unfavorable sequence of BMR emergences derails the buildup of the dipole in the descending phase of a cycle. Most often this involves

a single or a few high-flux BMR emerging with a E–W tilt pattern deviating strongly from Joy's law (see Nagy *et al.*, 2017). Recovery to "normal" cyclic behavior takes place through the agency of the deep-seated turbulent α-effect dynamo, as exemplified in Figure 2.

Under our modeling setup and parameter regime, a steady quadrupole is the fastest growing mode for an α-effect dynamo. As a consequence, the recovery from Grand Minima begins with the buildup of quadrupolar internal magnetic field, transiting to a mixed parity once the primary Babcock–Leighton dynamo begins to reactivate, and recovering dipolar parity once normal primary dynamo operation has resumed. The two Grand Minima in Figure 2 offer an example of this pattern, with emergences starting to occur in the northern hemisphere for a few decades before the failed restart at $t \approx 170$ years, and true restart at $t \approx 290$ years. This stands in qualitative agreement with sunspot observations during the Maunder Minimum (Ribes and Nesme-Ribes, 1993), which are most readily interpreted as resulting from a mixed-parity dynamo state (Sokoloff and Nesme-Ribes, 1994; Usoskin, Mursula, and Kovaltsov, 2000).

Parity modulation is most readily produced in nonlinear dynamo models including the magnetic backreaction on differential rotation (see, *e.g.*, Tobias, 1997; Beer, Tobias, and Weiss, 1998; Küker, Arlt, and Rüdiger, 1999; Moss and Brooke, 2000; Bushby, 2006). Here, in contrast, it materializes in a purely kinematic regime, from the interaction of two dynamos mechanisms operating under distinct saturation levels.

In this regime of mixed parity, our solar-cycle model can also transit to a dual-dynamo state which is the model's equivalent of a Grand Maximum. Observationally, Grand Maxima are harder to define than Grand Minima; in the case of the Maunder Grand Minimum a persistent dearth of sunspots is a clear criterion, but for Grand Maxima "significantly above normal levels" is quantitatively more ambiguous (Clette *et al.*, 2014; Usoskin, 2017), the exemplary case being the Modern Maximum (1940 – 2009 approximately). The reality of the Modern Maximum, which is the only example directly verifiable with sunspot data, is considered established *via* detailed observations of the Sun (Gibson, Zhao, and Fisk, 2011; Clette *et al.*, 2014; Zięba and Nieckarz, 2014; Usoskin *et al.*, 2016a). Cosmogenic-isotope data also reveal enhanced activity during this period, as well as the existence of other similar events throughout the Holocene (Usoskin, Mursula, and Kovaltsov, 2003; Solanki *et al.*, 2004; Inceoglu *et al.*, 2015).

Observationally, it remains unclear whether Grand Maxima correspond to a special state of the solar dynamo, or rather to the upper reaches of regular-cyclic activity (Usoskin, 2017). In contrast, in our simulations Grand Maxima can be identified unambiguously on the basis of the internal magnetic-field configurations. This is detailed in Figure 6, which closes in on a 300 years segment of the case-study simulation of Section 3, including a short Grand Minimum followed, upon exit, by the onset of a Grand Maximum. During Grand Maxima, the turbulent α-effect dynamo operates at elevated levels, almost on par with the primary Babcock–Leighton dynamo. This leads to the buildup of a steady, equatorially symmetric internal toroidal field at the base of the convection zone (Figure 6 fourth panel from top), which, in turn, generates a steady stream of BMR emergences at mid-latitudes, so that elevated PSSN counts are sustained even in the minimum phase of the primary dynamo (Figure 6 top panel). This represents a discrepancy between our simulation and the Modern Maximum, during which the real sunspot number reached values close to zero between successive activity cycles.

Comparison of this figure (and other similar Grand Maximum episodes) with the corresponding time interval on Figure 4 indicates that they are well delineated by a smoothed PSSN count of about 75. The corresponding threshold value is indicated by the red vertical line segment on the smoothed PSSN histogram of Figure 5. Based on this criterion,

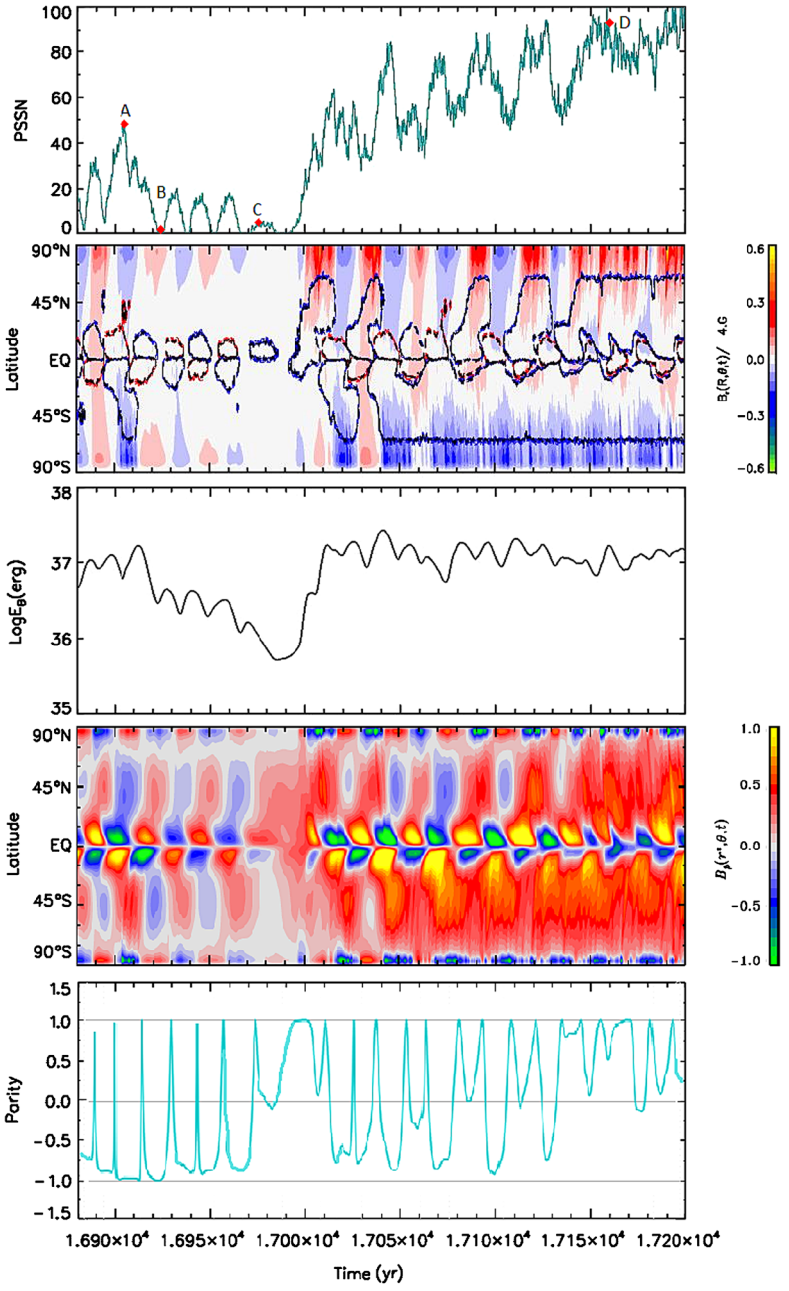

Figure 6 From *top* to *bottom*: PSSN time series with times labeled A, B, C, D corresponding, respectively, to epochs of primary cycle maximum, minimum, a Grand Minimum, and a Grand Maximum; the *second panel* is a time–latitude diagram of the zonally averaged surface radial field, with superimposed isocontours of BMR emergence density; the *third panel* a time series of total magnetic energy; the *fourth panel* a time–latitude diagram of the axisymmetric toroidal field at $r = 0.7$ $R_\odot$; and the *bottom panel* shows a time series of solution parity P, as defined in Equation 11, values of -1 $(+1)$ corresponding to dipole-like (quadrupole-like) magnetic configurations. This segment is extracted from our case-study simulation in Figure 4 and shows a "normal" dynamo behavior, a short Grand Minimum, followed by a Grand Maximum state (see text).

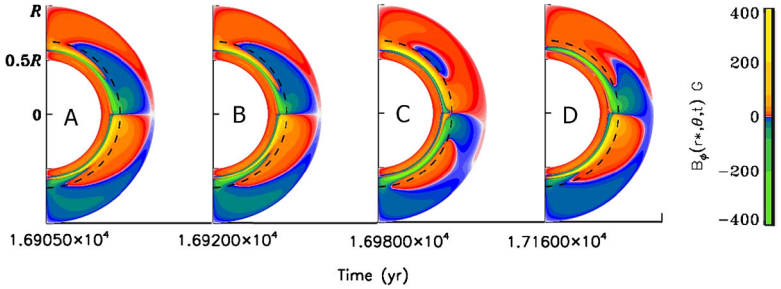

Figure 7 Meridional plane snapshots of the interior axisymmetric toroidal magnetic-field component at epochs labeled **A**, **B**, **C**, and **D** on the *top panel* of Figure 6. These correspond to a maximum (**A**) and minimum (**B**) of the primary cycle during normal cyclic operation, the end of a short Grand Minimum (**C**), and a Grand Maximum (**D**). The later two snapshots show marked departure from equatorially antisymmetric parity (see text).

84 Grand Maxima can be identified in the 50,000-year simulation of Figure 4, with a total duration of around 5250 years; the simulation thus spends around 10.2% of its time in an elevated active state.

Figure 7 illustrates the internal toroidal-field distribution plotted in the meridional plane, for the four epochs labeled A through D on Figure 6. Snapshots A and B are, respectively, at a maximum and minimum phase of the primary cycle during "normal" cyclic activity. Snapshot C is extracted during the brief Grand Minimum spanning here three cycles. Snapshot D is extracted near the peak of the Grand Maximum episode that follows recovery from the short Grand Minimum. The internal toroidal field is almost perfectly equatorially antisymmetric in snapshots A and B, as expected if the primary Babcock–Leighton dynamo dominates. Snapshot C shows significantly weaker fields, as well as a significant departure from pure antisymmetric parity. This departure is more pronounced, and the field strength much larger, during the Grand Maximum episode from which snapshot D is extracted. This mixed-parity dual-dynamo mode results here from a form of constructive interference between the primary Babcock–Leighton dynamo, and the deep-seated turbulent dynamo.

4. Statistical Properties of Grand Minima and Maxima

Having established criteria allowing the identification of Grand Minima and Maxima in our simulations, we can now turn to their statistical properties. The mean duration of Grand Minimum in the "case study" simulation is 67.57 years: quite close to the mean duration of 80 years extracted from activity timeseries reconstructed from cosmogenic-isotope data (Usoskin, Solanki, and Kovaltsov, 2007). Additionally, the recent analysis presented by Usoskin *et al.* (2016b) indicates that two to three Grand Minima occur every 1000 years, similar to the occurrence frequency measured in our simulation.

Figure 8 shows frequency distributions of Grand Minima and Maxima, as extracted from our case study simulation. Even with a 50,000-year simulation with 102 Grand Minima, the distributions remains irregular. We do note a hint of possible bimodality in the distribution of Grand Minima durations, with a few Grand Minima lasting a few centuries and a more numerous population of Grand Minima lasting under one century. Note also that the 30 – 60-year bin is by far the most populated. Grand Maxima appear to have a more regular distribution, falling more smoothly from decades to centuries, but again the relatively small number of events (84) yields a sparsely populated histogram.

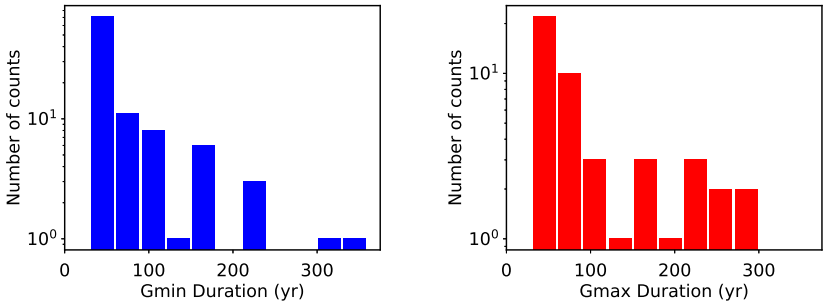

Figure 8 Grand Minima and Maxima duration histograms constructed with 102 Grand Minima and 84 Grand Maxima in the time series shown in Figure 4.

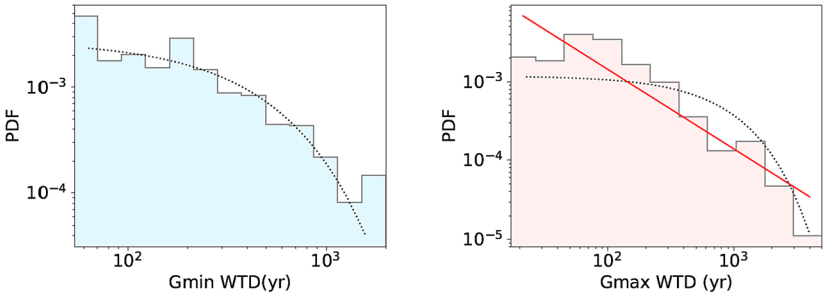

Figure 9 Probability density functions of waiting-time distributions (WTD) of Grand Minima (*left*) and Grand Maxima (*right*) in the time series shown in Figure 4. The *dotted lines* represent an exponential distribution while the *red line* indicates a power-law distribution.

4.1. Waiting Time Distributions (WTD)

The waiting time is defined as the time elapsed between two consecutive events. The probability distributions of the waiting times for Grand Minima and Maxima are shown on Figure 9. A stationary, memoryless, random (Poisson) process is expected to lead to an exponential WTD, while departure from such a distribution may indicate non-stationary or memory-bearing stochastic processes (Wheatland, 2000, 2003; Lepreti, Carbone, and Veltri, 2001; Solanki *et al.*, 2004; Usoskin, Solanki, and Kovaltsov, 2007; Clauset, Shalizi, and Newman, 2009; Inceoglu, Arlt, and Rempel, 2017). In particular, power-law WTDs are usually indicative of scale-free temporal correlations. The black solid lines in Figure 9 are least-squares fits to an exponential form, while the red line on the right panel is a power-law fit. All histogram bins were used in these fits, the point being simply to ascertain the general form of the two WTDs. Here an exponential fit yields an acceptable representation of the Grand Minima WTD, while for the Grand Maxima WTD a power-law form yields a somewhat better fit, although from a strictly statistical point of view an exponential form cannot be ruled out. Also statistically marginal but still noteworthy is the markedly elevated count in the first bin of the Grand Minima WTD (note that the vertical axis is logarithmic), a possible indication of mild clustering of events. These various properties are all qualitatively similar to those characterizing the corresponding distributions inferred from cosmogenic-isotope data (Usoskin, Solanki, and Kovaltsov, 2007).

In our basic dynamo model, Grand Minima are triggered by one or more "rogue" active regions with high magnetic fluxes and tilts departing strongly from Joy's law (Wang and Sheeley, 1991; Yeates, Baker, and van Driel-Gesztelyi, 2015; Nagy *et al.*, 2017). Tilts are ascribed to each emerging BMR by random draws from a stationary empirical distributions built from Cycle 21 magnetographic data (see Lemerle, Charbonneau, and Carignan-Dugas, 2015, Appendix, for details). Under these conditions an exponential WTD is in fact expected. Exit from Grand Minima is a deterministic process, as it is set by the growth rate of the secondary turbulent dynamo, as well as the overall internal magnetic-field distribution at the time of onset. Event-to-event variations in the internal field distribution is ultimately responsible for the relatively wide spread of Grand Minima durations characterizing our simulations.

The non-exponential form of the Grand Maxima WTD is compatible with the idea that the latter result from a mechanism that is not completely stochastic. We identified Grand Maxima as resulting from a form of constructive interference between the primary dynamo and the secondary turbulent dynamo. Changes in the internal distribution of magnetic fields, particularly at and below the base of the convection presumably driven by stochastic effects, allow comparatively stronger quenching of the Babcock–Leighton mechanism, with the inductive induction of the α-effect then becoming comparable, yielding a true dual dynamo. Support for this interpretation is found in the internal magnetic-field distribution (Figure 7), as well as in the varying equatorial parity in going from normal cyclic activity to Grand Maxima state (Figure 6, bottom panel).

4.2. Quasi-Periodicity Analysis

Visual examination of Figure 4 suggests that Grand Minima and Maxima do not recur periodically, and that a Grand Minimum need not be necessarily followed by a Grand Maximum, and *vice versa*; the extended Grand Maximum immediately following the short Grand Minimum on Figure 6 is not at all the rule in this respect. Nonetheless the presence of long periodicities or quasi-periodicities cannot be ruled out on such a purely visual basis.

Figure 10 presents a Morlet wavelet analysis of the 50,000-year smoothed PSSN time series of Figure 4, performed using the WAIPY package (Calim Costa, 2013). The right frame shows a standard Fourier spectrum, as well as the Morlet spectrum resulting from time integration of the wavelet power distribution. Because the time series results from 1-2-2-2-1 smoothing of a series of decadal sampling, the primary 11-year half-cycle is not expected to show up with significant amplitude in these various spectra. The most striking pattern in the wavelet power distribution is observed in the period range of 1000 – 3000 years, where intermittently recurring power structures are clearly visible, adding up to statistically significant peaks in the time-integrated power spectra at the right.

With the existence of a recurring quasi-periodicity in the 1000 – 3000-year period range thus established, a closer examination of Figure 4 reveals a tendency for groups of three to four extended Grand Maxima to cluster with a commensurate spacing of 1000 – 3000 years, these clusters being separated by some 8000 years. This longer recurrence period corresponds, again roughly, to the power structure at the longest periods accessible to the wavelet analysis of Figure 10, but a much longer simulation is required to firmly establish its quasi-period. This clustering of Grand Maxima is consistent with the non-exponential form of their waiting-time distribution (*viz.* Figure 9). There is again qualitative similarity with the cosmogenic radioisotope reconstructions of Usoskin *et al.* (2016b), who offer evidence that Grand Minima and Maxima occur aperiodically, but with a tendency for clustering, respectively, near lows and highs of the Hallstatt cycle (2300 – 2400-year period range).

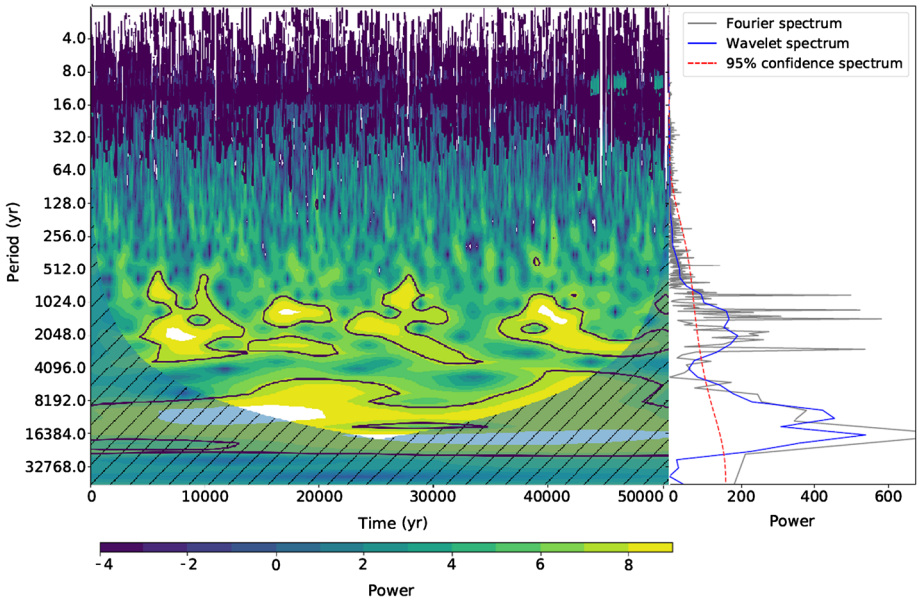

Figure 10 *Left*: Morlet wavelet spectrum of the smoothed PSSN time series of Figure 4 for a solution with $K = 0.32$, $\alpha_0 = -12$ cm s^{-1}, $B_0 = 210$ G, $B_q = 120$ G, $\eta_c = 10^8$ cm^2 s^{-1}, $\eta_t = 10^{11.8}$ cm^2 s^{-1}. Note the irregular waxing and waning of power in the 1000 – 3000-year period range. The hatched area is not statistically significant. The *right panel* shows the time-integrated Morlet spectrum (in *blue*) with the 95% confidence level indicated by the *red dashed line*, along with a standard Fourier spectrum (in *gray*).

However, in contrast to these reconstructions, we find no hints of Gleissberg-like periodicity (80 – 100 years) in the wavelet transform or Fourier spectra.

The only millennial timescale present within our solar-cycle model is associated with magnetic diffusion in the layers underlying the convection zone within which the bulk of dynamo action is taking place. The best-fit reference model of LC17 is characterized by a contrast of magnetic diffusivity of four orders of magnitude between the bottom of the domain $\eta_c = 10^8$ cm^2 s^{-1}, and its "convection zone", where convective turbulence is taken to generate a much stronger net diffusivity, $\eta_t = 10^{11.8}$ cm^2 s^{-1}, for the "case study" simulation presented here. Examination of the dynamo solution reveals the buildup of intense magnetic fields immediately beneath the convection zone, concentrated in a region of radial extent $r/R_\odot \approx 0.05$ (see Figure 7). An estimate for the magnetic dissipation time of such a structure is $\tau = (0.05\ R_\odot)^2/\eta_c \approx 3900$ years. One can conjecture that the buildup of this layer is triggered by a cycle of particularly high amplitude, again resulting from stochasticity in BMR emergences, pushing the system in the dual-dynamo state persisting for a time of the order of the diffusive decay time for the participating deep-seated magnetic layer. Support for this conjecture is found in the fact that the power peaks at long periods in the wavelength transform shifts to shorter periods as the core diffusivity is increased to $\eta_c = 10^9$ cm^2 s^{-1}, and they vanish as η_c exceeds 10^{10} cm^2 s^{-1}.

5. Parameter Dependencies

The "case study" solution discussed in the preceding section was selected among a vast number of simulations computed under different parameter regimes. The parameter being

Table 1 Parametrized variables in the model.

Parameters	Physical meaning	Tested Interval	LC17	Section 3
K	Strength of primary BL dynamo	[0.15, 1.20]	–	0.32
B_q	Threshold field for tilt quenching [G]	[100, 500]	–	120
$\log(\eta_c)$	Diffusivity in the core [$cm^2\,s^{-1}$]	[7, 11]	$8.0\pm^{2.4}_{1.0}$	8
$\log(\eta_t)$	Envelope turbulent diffusivity [$cm^2\,s^{-1}$]	[11.0, 13.0]	$12.0\pm^{0.2}_{0.4}$	11.8
B_0	Threshold toroidal field [G]	[100, 1000]	N/A	210
α_0	Strength of turbulent dynamo [$cm\,s^{-1}$]	[−25, −9]	N/A	−12

varied, and their ranges of variations, are listed in Table 1. The first is the one free parameter of the LC17 model, namely the dynamo number controlling the rate of BMR emergences as a function of the internal magnetic-field strength. The following three are structural parameters of the basic LC17 model, and they were only varied within the range allowed by the optimization procedure. The last two are characterizing the strength and saturation-field strength for the turbulent α-effect. We have also explored varying spatial distribution for the α-effect, including a Northern Hemisphere positive α-effect distributed throughout the convection zone. For the (limited) range of such solutions explored, non-solar behavior invariably materializes in these cases.

The effects of changes in these parameter on the occurrence and characteristics of Grand Minima and Maxima can be summarized as follows:

- As the primary dynamo number [K] increases, the primary dynamo spends more time in "normal" cyclic operation, and the number of Grand Minima decreases. The BL dynamo operates at a high energy level and the frequency of Grand Maxima increases.
- At low K, the dynamo produces Grand Minima more frequently and operates at low energy level, and Grand Maxima become very rare.
- The parameter α_0 sets the overall magnitude of the alpha effect. Close to its critical value ($\alpha_{crit} \approx -9\ cm\,s^{-1}$), turbulent induction cannot offset magnetic dissipation, and the BL dynamo never restarts once it stops. Running significantly above critical allows restart, but above $\alpha_0 \approx -25$ the turbulent dynamo dominates, and non-solar behavior typically ensues.
- The parameter B_0 is the toroidal magnetic-field strength at which quenching of the turbulent α-effect becomes important. The adopted algebraic quenching formula Equation 9 is entirely *ad hoc*. The key is to pick a value low enough that normal operation of the primary Babcock–Leighton dynamo strongly quenches the α-effect, but still high enough to allow the α-effect to amplify the magnetic field back above the emergence threshold of the Babcock–Leighton dynamo. This desired behavior materializes only on a fairly restricted range of quenching field strength, otherwise non-solar behavior again ensues. Within this range, lowering the threshold B_0 lowers the overall magnetic energy during "normal" cyclic operation, and Grand Minima become longer. On the other hand, increasing B_0 leads to shorter and more frequent Grand Minima.
- Increasing the core diffusivity [η_c] decreases the efficiency of the deep-seated α-effect dynamo, and leads to longer quiescent episodes around the model's critical operation level when K is between 0.25 and 0.35.
- Everything else being equal, the ratio K/α_0 measures the relative importance of the two inductive mechanisms for the poloidal magnetic component that are operating within the model. However, in itself this ratio does not provide a useful discriminant of intermittency behavior as other parameters are varied.

6. Discussion and Conclusion

In this article we have described the addition of a turbulent electromotive force, in the form of the mean-field α-effect, into the kinematic 2×2D Babcock–Leighton solar-cycle model of Lemerle and Charbonneau (2017). This addition was motivated by the need to "jumpstart" the Babcock–Leighton dynamo after the internal magnetic field falls below the field-strength threshold allowing the formation and emergence of bipolar magnetic regions. In the resulting dual-dynamo model, stochastic fluctuations in properties of emerging bipolar magnetic regions can trigger extended periods of strongly reduced activity, the model's equivalent of Grand Minima, recovery to normal cyclic behavior being driven by the α-effect. We also showed that interaction between the deep-seated, weak turbulent dynamo and the surface Babcock–Leighton mechanism can generate a hybrid dynamo mode characterized by extended periods of markedly above-average activity, which become the model's equivalent of Grand Maxima.

The many adjustable parameters in the Lemerle and Charbonneau (2017) models were formally optimized to match the sunspot butterfly diagram, and these optimal values were retained in most simulations reported upon in this article. Two new parameters were introduced to control the behavior of the turbulent α-effect: a dynamo number measuring its strength, and a quenching field strength determining its saturation level. This secondary dynamo number is set as low as possible so as to avoid perturbing the normal operation of the primary Babcock–Leighton dynamo, the idea being that the secondary turbulent dynamo makes a significant inductive contribution only when its Babcock–Leighton counterparts falls below threshold. Straightforward as this may sound, it required a relatively fine tuning of the saturation threshold for the α-effect. Nevertheless, after parameter tuning, the resulting dual-dynamo model succeeds in generating irregularly occurring Grand Minima and Maxima, with distributions of durations and inter-event waiting times remarkably similar to the corresponding distributions inferred from the cosmogenic-isotope record.

Solar-like long-timescale behavior does require here a relatively fine tuning of the parameters defining the strength and quenching of the α-effect. Hazra, Passos, and Nandy (2014) encountered a similar need for fine tuning in their own dual-dynamo model of Grand Minima. It is quite conceivable that a more robust parameter set could be uncovered by repeating, with all parameters of our dual-dynamo model, the formal optimization procedure used in LC17. This being a very computationally intensive endeavor, we have opted to postpone it to a follow-up investigation, in the course of which a wider variety of spatial distributions for the turbulent α-effect and meridional-flow configurations will also be explored.

In the model, Grand Minima are triggered following the emergence of one or more high-flux active regions having unusual tilt angles, derailing the buildup of the surface dipole and leading to the subsequent shutdown of the primary cycle. This phenomenon is investigated in detail by Nagy *et al.* (2017, see also Karak and Miesch 2018). Because active-region properties are drawn randomly from stationary distributions of values built from observations, the onset of Grand Minima is a truly memoryless random process, leading to an exponential distribution of inter-event waiting time. Recovery from Grand Minima is achieved through the inductive action of the low-amplitude turbulent α-effect, so that the mean duration of Grand Minima is set primarily by the growth rate of the associated dynamo, itself determined by the adopted value for the dynamo number: the higher this value, the shorter the mean duration of Grand Minima.

Because the secondary α-effect dynamo generates a steady, equatorially symmetric magnetic field in the parameter regime considered here, the exit from Grand Minima is characterized by a mixed-parity state, in qualitative agreement with sunspot observations in the second half of the Maunder Minimum (Ribes and Nesme-Ribes, 1993).

It is instructive to compare our results to those presented by Karak and Miesch (2018). These authors succeed in generating Grand Minima in their Babcock–Leighton-type 3D solar-cycle model without an additional inductive mechanism, even though their model, like ours, includes a threshold on BMR emergences. Examination of their dynamo solutions (see their Figure 2), however, suggests that their threshold value is such that many BMR emergences continue to take place during events that they identify as Grand Minima, so that the primary cycle never stops. This is quite distinct from the situation encountered with our model, in which BMR emergences cease completely for time intervals much longer than the primary cycle period (*cf.* Figure 2 of Karak and Miesch 2018 and Figure 2 herein).

Grand Maxima arise in our model as a truly distinct mixed-dynamo state of mixed parity, in which the deep-seated α-effect and the surface Babcock–Leighton effect contribute more or less equally to the regeneration of the poloidal large-scale magnetic field *via* a form of constructive interference. Analyses of the simulation results reveal a non-exponential waiting-time distribution for such Grand Maxima events, suggesting that deterministic effects operating on long timescales contribute to their temporal recurrence pattern. Detection of spectral power in the 1000 – 3000-year range, also recurring in the wavelet transform, supports this idea. In our kinematic model, the only commensurate timescale is associated with magnetic dissipation in the stable, low magnetic-diffusivity layer underlying the high-diffusivity "convection zone" at the base of which the α-effect is operating. This suggests that the slow dissipation of magnetic fields sometimes building up in this deep layer sets this long timescale, over which the dominance of the deep-seated turbulent dynamo waxes and wanes.

We are not claiming that the specific hybrid dynamo model described here is a physically accurate representation of the real dynamo processes taking place in the solar interior. However, our model does show that even in the kinematic regime, short-timescale random fluctuations occurring naturally within the Babcock–Leighton mechanism can lead to systematic variations on very long timescales, including solar-like Grand Minima, Grand Maxima, and quasi-periodicities in the millennia range that resemble at least qualitatively inferred solar behavior. The occurrence of long quasi-periodicities is particularly noteworthy, as this is usually difficult to generate *via* stochastic driving alone, and *is* typically ascribed to deterministic nonlinear magnetic backreaction of large-scale flows, particularly differential rotation (see, *e.g.*, Tobias, 1997; Beer, Tobias, and Weiss, 1998; Küker, Arlt, and Rüdiger, 1999; Moss and Brooke, 2000; Bushby, 2006). Our results indicate that interaction between distinct dynamo mechanisms can achieve the same effect, while generating statistical distributions of Grand Minima and Maxima events consistent with solar-activity reconstructions based on the cosmogenic-isotope record. Introduction of dynamical backreaction on differential rotation is an obvious next step in further development of the model, as the cited non-kinematic studies have shown that this can naturally lead to intermediate, Gleissberg-like centennial quasi-periodicities, which our current model does not appear capable of generating.

Acknowledgements This work was supported by the Discovery Grant Program of Canada's Natural Sciences and Engineering Research Council. Special thanks to Ilya G. Usoskin for kindly providing their most recent reconstructed solar-activity time series based on ^{10}Be and ^{14}C cosmogenic radioisotopes.

Conflict of interest The authors declare that they have no conflicts of interest.

References

Augustson, K., Brun, A.S., Miesch, M., Toomre, J.: 2015, Grand minima and equatorward propagation in a cycling stellar convective dynamo. *Astrophys. J.* **809**, 149. DOI. ADS.

Baumann, I., Schmitt, D., Schüssler, M., Solanki, S.K.: 2004, Evolution of the large-scale magnetic field on the solar surface: a parameter study. *Astron. Astrophys.* **426**, 1075. DOI. ADS.

Beer, J., Tobias, S., Weiss, N.: 1998, An active sun throughout the maunder minimum. *Solar Phys.* **181**, 237. DOI. ADS.

Beer, J., Blinov, A., Bonani, G., Finkel, R.C., Hofmann, H.J., Lehmann, B., Oeschger, H., Sigg, A., Schwander, J., Staffelbach, T., Stauffer, B., Suter, M., Wötfli, W.: 1990, Use of Be-10 in polar ice to trace the 11-year cycle of solar activity. *Nature* **347**, 164. DOI. ADS.

Bushby, P.J.: 2006, Zonal flows and grand minima in a solar dynamo model. *Mon. Not. Roy. Astron. Soc.* **371**, 772. DOI. ADS.

Caligari, P., Moreno-Insertis, F., Schüssler, M.: 1995, Emerging flux tubes in the solar convection zone. 1: asymmetry, tilt, and emergence latitude. *Astrophys. J.* **441**, 886. DOI. ADS.

Calim Costa, M.: 2013, WAIPY, wavelet analysis in Python.

Cameron, R.H., Schüssler, M.: 2012, Are the strengths of solar cycles determined by converging flows towards the activity belts? *Astron. Astrophys.* **548**, A57. DOI. ADS.

Cameron, R.H., Schüssler, M.: 2017, Understanding solar cycle variability. *Astrophys. J.* **843**, 111. DOI. ADS.

Cameron, R.H., Jiang, J., Schmitt, D., Schüssler, M.: 2010, Surface flux transport modeling for solar cycles 15 – 21: effects of cycle-dependent tilt angles of sunspot groups. *Astrophys. J.* **719**, 264. DOI. ADS.

Charbonneau, P.: 2010, Dynamo models of the solar cycle. *Liv. Rev. Solar Phys.* **7**, 3. DOI. ADS.

Charbonneau, P.: 2014, Solar dynamo theory. *Annu. Rev. Astron. Astrophys.* **52**, 251. DOI. ADS.

Charbonneau, P., Blais-Laurier, G., St-Jean, C.: 2004, Intermittency and phase persistence in a Babcock–Leighton model of the solar cycle. *Astrophys. J. Lett.* **616**, L183. DOI. ADS.

Clauset, A., Shalizi, C.R., Newman, M.E.J.: 2009, Power-law distributions in empirical data. *SIAM Rev.* **51**, 661. DOI. ADS.

Clette, F., Svalgaard, L., Vaquero, J.M., Cliver, E.W.: 2014, Revisiting the sunspot number. A 400-year perspective on the solar cycle. *Space Sci. Rev.* **186**, 35. DOI. ADS.

Dikpati, M., Charbonneau, P.: 1999, A Babcock–Leighton flux transport dynamo with solar-like differential rotation. *Astrophys. J.* **518**, 508. DOI. ADS.

D'Silva, S., Howard, R.F.: 1993, Limits on the magnetic field strength at the base of the solar convection zone. *Solar Phys.* **148**, 1. DOI. ADS.

Eddy, J.A.: 1976, The Maunder minimum. *Science* **192**, 1189. DOI. ADS.

Fan, Y.: 2009, The emergence of a twisted flux tube into the solar atmosphere: sunspot rotations and the formation of a coronal flux rope. *Astrophys. J.* **697**, 1529. DOI. ADS.

Gibson, S.E., Zhao, L., Fisk, L.A.: 2011, The solar wind structure and heliospheric magnetic field in the solar Cycle 23 – 24 minimum and in the increasing phase of Cycle 24. In: *AGU Fall Meeting Abstracts, SH31D*. ADS.

Gleissberg, W.: 1944, A secular change in the shape of the spot-frequency curve. *Observatory* **65**, 244. ADS.

Hathaway, D.H.: 2009, Solar cycle forecasting. *Space Sci. Rev.* **144**, 401. DOI. ADS.

Hazra, S., Passos, D., Nandy, D.: 2014, A stochastically forced time delay solar dynamo model: self-consistent recovery from a maunder-like grand minimum necessitates a mean-field alpha effect. *Astrophys. J.* **789**, 5. DOI. ADS.

Inceoglu, F., Arlt, R., Rempel, M.: 2017, The nature of grand minima and maxima from fully nonlinear flux transport dynamos. *Astrophys. J.* **848**, 93. DOI. ADS.

Inceoglu, F., Simoniello, R., Knudsen, M.F., Karoff, C., Olsen, J., Turck-Chiéze, S., Jacobsen, B.H.: 2015, Grand solar minima and maxima deduced from ^{10}Be and ^{14}C : magnetic dynamo configuration and polarity reversal. *Astron. Astrophys.* **577**, A20. DOI. ADS.

Jiang, J., Cameron, R.H., Schüssler, M.: 2015, The cause of the weak solar Cycle 24. *Astrophys. J.* **808**, L28. DOI. ADS.

Jiang, J., Hathaway, D.H., Cameron, R.H., Solanki, S.K., Gizon, L., Upton, L.: 2014, Magnetic flux transport at the solar surface. *Space Sci. Rev.* **186**, 491. DOI. ADS.

Käpylä, M.J., Käpylä, P.J., Olspert, N., Brandenburg, A., Warnecke, J., Karak, B.B., Pelt, J.: 2016, Multiple dynamo modes as a mechanism for long-term solar activity variations. *Astron. Astrophys.* **589**, A56. DOI. ADS.

Karak, B.B., Miesch, M.: 2017, Solar cycle variability induced by tilt angle scatter in a Babcock–Leighton solar dynamo model. *Astrophys. J.* **847**, 69. DOI. ADS.

Karak, B.B., Miesch, M.: 2018, Recovery from Maunder-like grand minima in a Babcock–Leighton solar dynamo model. *Astrophys. J. Lett.* **860**, L26. DOI. ADS.

Karak, B.B., Jiang, J., Miesch, M.S., Charbonneau, P., Choudhuri, A.R.: 2014, Flux transport dynamos: from kinematics to dynamics. *Space Sci. Rev.* **186**, 561. DOI. ADS.

Knudsen, M.F., Riisager, P., Jacobsen, B.H., Muscheler, R., Snowball, I., Seidenkrantz, M.-S.: 2009, Taking the pulse of the Sun during the Holocene by joint analysis of ^{14}C and ^{10}Be. *Geophys. Res. Lett.* **36**, L16701. DOI. ADS.

Krause, F., Rädler, K.-H.: 1980, *Mean-Field Magnetohydrodynamics and Dynamo Theory*. Pergamon, Oxford. ADS.

Küker, M., Arlt, R., Rüdiger, G.: 1999, The Maunder minimum as due to magnetic Lambda -quenching. *Astron. Astrophys.* **343**, 977. ADS.

Lemerle, A., Charbonneau, P.: 2017, A coupled 2×2D Babcock–Leighton solar dynamo model. II. Reference dynamo solutions. *Astrophys. J.* **834**, 133. DOI. ADS.

Lemerle, A., Charbonneau, P., Carignan-Dugas, A.: 2015, A coupled 2×2D Babcock–Leighton solar dynamo model. I. Surface magnetic flux evolution. *Astrophys. J.* **810**, 78. DOI. ADS.

Lepreti, F., Carbone, V., Veltri, P.: 2001, Solar flare waiting time distribution: varying-rate Poisson or Lévy function? *Astrophys. J.* **555**, L133. DOI. ADS.

McClintock, B.H., Norton, A.A.: 2013, Recovering joy's law as a function of solar cycle, hemisphere, and longitude. *Solar Phys.* **287**, 215. DOI. ADS.

Moss, D., Brooke, J.: 2000, Towards a model for the solar dynamo. *Mon. Not. Roy. Astron. Soc.* **315**, 521. DOI. ADS.

Mursula, K., Ulich, T.: 1998, A new method to determine the solar cycle length. *Geophys. Res. Lett.* **25**, 1837. DOI. ADS.

Nagy, M., Lemerle, A., Labonville, F., Petrovay, K., Charbonneau, P.: 2017, The effect of "rogue" active regions on the solar cycle. *Solar Phys.* **292**, 167. DOI. ADS.

Ossendrijver, M.A.J.H.: 2000, Grand minima in a buoyancy-driven solar dynamo. *Astron. Astrophys.* **359**, 364. ADS.

Parker, E.N.: 1955, Hydromagnetic dynamo models. *Astrophys. J.* **122**, 293. DOI. ADS.

Passos, D., Nandy, D., Hazra, S., Lopes, I.: 2014, A solar dynamo model driven by mean-field alpha and Babcock–Leighton sources: fluctuations, grand-minima-maxima, and hemispheric asymmetry in sunspot cycles. *Astron. Astrophys.* **563**, A18. DOI. ADS.

Petrovay, K.: 2010, Solar cycle prediction. *Liv. Rev. Solar Phys.* **7**, 6. DOI. ADS.

Pipin, V.V., Kosovichev, A.G.: 2011, Mean-field solar dynamo models with a strong meridional flow at the bottom of the convection zone. *Astrophys. J.* **738**, 104. DOI. ADS.

Ribes, J.C., Nesme-Ribes, E.: 1993, The solar sunspot cycle in the Maunder minimum AD1645 to AD1715. *Astron. Astrophys.* **276**, 549. ADS.

Sanchez, S., Fournier, A., Aubert, J.: 2014, The predictability of advection-dominated flux-transport solar dynamo models. *Astrophys. J.* **781**, 8. DOI. ADS.

Sokoloff, D., Nesme-Ribes, E.: 1994, The Maunder minimum: a mixed-parity dynamo mode? *Astron. Astrophys.* **288**, 293. ADS.

Solanki, S.K., Usoskin, I.G., Kromer, B., Schüssler, M., Beer, J.: 2004, Unusual activity of the Sun during recent decades compared to the previous 11,000 years. *Nature* **431**, 1084. DOI. ADS.

Steinhilber, F., Abreu, J.A., Beer, J., Brunner, I., Christl, M., Fischer, H., Heikkila, U., Kubik, P.W., Mann, M., McCracken, K.G., Miller, H., Miyahara, H., Oerter, H., Wilhelms, F.: 2012, 9,400 years of cosmic radiation and solar activity from ice cores and tree rings. *Proc. Indian Natl. Sci.* **109**, 5967. DOI. ADS.

Svalgaard, L., Cliver, E.W., Kamide, Y.: 2005, Sunspot cycle 24: smallest cycle in 100 years? *Geophys. Res. Lett.* **32**, L01104. DOI. ADS.

Tobias, S.M.: 1997, The solar cycle: parity interactions and amplitude modulation. *Astron. Astrophys.* **322**, 1007. ADS.

Usoskin, I.G.: 2013, A history of solar activity over millennia. *Liv. Rev. Solar Phys.* **10**, 1. DOI. ADS.

Usoskin, I.G.: 2017, A history of solar activity over millennia. *Liv. Rev. Solar Phys.* **14**, 3. DOI. ADS.

Usoskin, I.G., Mursula, K., Kovaltsov, G.A.: 2000, Regular and random components of sunspot activity during active sun and great minima: model simulation. In: Wilson, A. (ed.) *The Solar Cycle and Terrestrial Climate, Solar and Space Weather*, **SP-463**, ESA, Noordwijk, 447. ADS.

Usoskin, I.G., Mursula, K., Kovaltsov, G.A.: 2003, Reconstruction of monthly and yearly group sunspot numbers from sparse daily observations. *Solar Phys.* **218**, 295. DOI. ADS.

Usoskin, I.G., Solanki, S.K., Kovaltsov, G.A.: 2007, Grand minima and maxima of solar activity: new observational constraints. *Astron. Astrophys.* **471**, 301. DOI. ADS.

Usoskin, I.G., Hulot, G., Gallet, Y., Roth, R., Licht, A., Joos, F., Kovaltsov, G.A., Thébault, E., Khokhlov, A.: 2014, Evidence for distinct modes of solar activity. *Astron. Astrophys.* **562**, L10. DOI. ADS.

Usoskin, I.G., Kovaltsov, G.A., Lockwood, M., Mursula, K., Owens, M., Solanki, S.K.: 2016a, A new calibrated sunspot group series since 1749: statistics of active day fractions. *Solar Phys.* **291**, 2685. DOI. ADS.

Usoskin, I.G., Gallet, Y., Lopes, F., Kovaltsov, G.A., Hulot, G.: 2016b, Solar activity during the Holocene: the Hallstatt cycle and its consequence for grand minima and maxima. *Astron. Astrophys.* **587**, A150. DOI. ADS.

Vecchio, A., Lepreti, F., Laurenza, M., Alberti, T., Carbone, V.: 2017, Connection between solar activity cycles and grand minima generation. *Astron. Astrophys.* **599**, A58. DOI. ADS.

Wang, Y.-M., Lean, J., Sheeley, N.R. Jr.: 2002, Role of a variable meridional flow in the secular evolution of the Sun's polar fields and open flux. *Astrophys. J. Lett.* **577**, L53. DOI. ADS.

Wang, Y.-M., Sheeley, N.R. Jr.: 1991, Magnetic flux transport and the sun's dipole moment – new twists to the Babcock–Leighton model. *Astrophys. J.* **375**, 761. DOI. ADS.

Wheatland, M.S.: 2000, The origin of the solar flare waiting-time distribution. *Astrophys. J. Lett.* **536**, L109. DOI. ADS.

Wheatland, M.S.: 2003, The coronal mass ejection waiting-time distribution. *Solar Phys.* **214**, 361. DOI. ADS.

Whitbread, T., Yeates, A.R., Muñoz-Jaramillo, A., Petrie, G.J.D.: 2017, Parameter optimization for surface flux transport models. *Astron. Astrophys.* **607**, A76. DOI. ADS.

Yeates, A.R., Baker, D., van Driel-Gesztelyi, L.: 2015, Source of a prominent poleward surge during solar Cycle 24. *Solar Phys.* **290**, 3189. DOI. ADS.

Yeates, A.R., Muñoz-Jaramillo, A.: 2013, Kinematic active region formation in a three-dimensional solar dynamo model. *Mon. Not. Roy. Astron. Soc.* **436**, 3366. DOI. ADS.

Zięba, S., Nieckarz, Z.: 2014, Sunspot time series: passive and active intervals. *Solar Phys.* **289**, 2705. DOI. ADS.